The intrinsically disordered N-terminus of the voltage-dependent anion channel

Jordane Preto[a]*, and Isabelle Krimm[a,b]

[a]Université Claude Bernard Lyon 1, Centre de Recherche en Cancérologie de Lyon, INSERM 1052, CNRS 5286, Lyon, France

[b]CRMN, Université de Lyon, CNRS 5280, ENS de Lyon, 5 Rue de La Doua, F-69100, Villeurbanne, France.

* Corresponding author. E-mail: jordane.preto@univ-lyon1.fr

Abstract. The voltage-dependent anion channel (VDAC) is a critical β-barrel membrane protein of the mitochondrial outer membrane, which regulates the transport of ions and ATP between mitochondria and the cytoplasm. In addition, VDAC plays a central role in the control of apoptosis and is therefore of great interest in both cancer and neurodegenerative diseases. Although not fully understood, it is presumed that the gating mechanism of VDAC is governed by its N-terminal region which, in the open state of the channel, exhibits an α-helical structure positioned inside the pore and strongly interacting with the β-barrel wall.

In the present work, we combined molecular simulations with a recently developed force field for disordered systems to shed new light on known experimental results, showing that the N-terminus of VDAC is an intrinsically disordered region (IDR). First, simulation of the N-terminal segment as a free peptide highlighted its disordered nature and the importance of using an IDR-specific force field to properly sample its conformational landscape. Secondly, accelerated dynamics simulation of a double cysteine VDAC mutant under applied voltage revealed

a metastable low conducting state of the channel representative of closed states observed experimentally. Related structures were characterized by partial unfolding and rearrangement of the N-terminal tail that led to steric hindrance of the pore. Our results indicate that the disordered properties of the N-terminus are crucial to properly account for the gating mechanism of VDAC.

Author summary. The voltage-dependent anion channel (VDAC) is a membrane protein playing a pivotal role in the transport of ions or ATP across the mitochondrial outer membrane as well as in the induction of apoptosis. At high membrane potential, VDAC is known to transition from an open state to multiple closed states, reducing the flow of ions through the channel and blocking the passage of large metabolites. While the structure of the open state was resolved more than a decade ago, a molecular description of the gating mechanism of the channel is still missing. Here we show that the N-terminus of VDAC is an intrinsically disordered region and that such a property has a profound impact on its dynamics either as a free peptide or as part of the channel. By taking disordered properties of the N-terminus into account, we managed to simulate closure of the channel at experimental values of the membrane potential. Our results provide new insights into the molecular mechanism driving the gating process of VDAC.

1. Introduction

The voltage-dependent anion channel (VDAC) is a major porin located in the mitochondrial outer membrane (MOM). One of VDAC's main function is to mediate the transport of ions or small metabolites such as ATP, ADP or NADH between the mitochondrial intermembrane space (IMS) and the cytoplasm thus contributing to cell homeostasis (1). In addition, the channel is responsible for alteration of the permeability of the MOM which may result, under specific stimuli, to the release of apoptogenic factors like cytochrome C from the IMS, eventually

leading to apoptosis (2). Through its ability to interact with a dozen different proteins – including itself – VDAC was shown to either induce or inhibit apoptosis depending on its interaction partner (2). For this reason, VDAC is usually considered a promising target not only for cancer treatment but also in neurodegenerative diseases where the main goal is to prevent early stages of neuron's death (3).

Single-channel conductance experiments have revealed that VDAC can either be found in an open, high conducting, state prevailing at low membrane potential (between -30 mV and 30 mV) or in closed, low conducting, states occurring at more extreme voltage (above or below ± 30 mV) (4, 5). Importantly, anion selectivity can be relatively high in the open state (the anion/cation ratio is estimated around 5 at 150 mM KCl concentration) while closed states were reported to be cation selective (5, 6). Although the structure of the open state of VDAC was resolved more than a decade ago, little is known regarding the structure of the closed states due to their transient properties in normal conditions (4).

Experimental structures of the open state of VDAC were first released in 2008 by three separate groups using X-ray crystallography and/or NMR (7-9). VDAC is composed of 19 β-strands forming the barrel as well as an α-helical N-terminus (residues M1 to G25) located inside the pore and interacting with the barrel mostly via hydrophobic contacts (Fig 1). While the structure of the β-barrel was similar in all cases, slight differences in the position and in the α-helical content of the N-terminus, i.e., long helix vs. small helix vs. helix-break-helix, were observed between published structures (10). Although the N-terminus was reported to be stable in the open state (no large conformational change on the sub-millisecond timescale (11)), these slight variations may be an indicator of local flexibility of that region on longer timescales or different arrangements due to external conditions such as lipid environment (10). The mobility of the N-terminus was confirmed in a wide range of biophysical studies suggesting that the segment could detach from the pore and even translocate outside the channel during voltage

gating (12). Nevertheless, N-terminal translocation does not seem to be required for gating as several experimental studies introducing a disulfide bridge to "lock" the N-terminus against the β-barrel wall showed that closed states may still arise when the segment is located inside the pore (13, 14). Such studies include that of Teijido and al. (14) where the introduction of a S-S bond at L10C-A170C was found to have no effect on the conductance profile of the channel confirming that closure can still be induced without any large conformational change of the N-terminus.

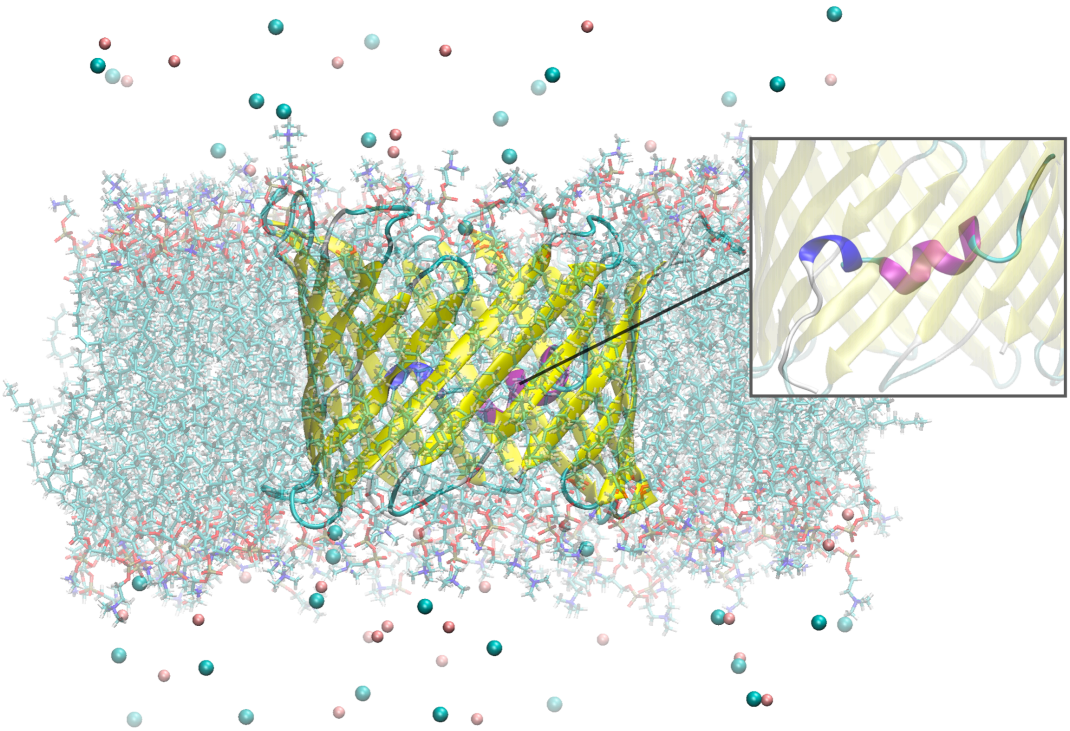

Fig 1. VDAC embedded in a lipid bilayer. The structure of the murine VDAC1 (mVDAC1) solved by X-ray crystallography was used (PDB ID: 3EMN (9)). The inset shows a closer view of the N-terminal region with the 3-10 helix involving Y7, A8 and D9, depicted in dark blue, and the standard helix (residues K12 to T19) in dark pink. Chloride and potassium ions (at a 150-mM KCl concentration) are also shown for illustrative purposes.

Finally, important structural properties of the N-terminus of VDAC were discovered by De Pinto and coworkers (15, 16). Using NMR and circular dichroism (CD) experiments, the authors found that the N-terminal fragment, when produced as a free peptide in solution, was

89 characterized by no apparent structural content. From molecular dynamics (MD) simulations,
90 it was proposed that such a peptide could exist in a dynamic equilibrium alternating between
91 random coil and α-helix content while interaction of the N-terminal region with the inner part
92 of the VDAC barrel would "choose" the α-helix conformation over unstructured ones (16).

93 In the present paper, it is shown that the lack of apparent structure experimentally ob-
94 served by De Pinto and coworkers is a simple illustration of the disordered nature of the N-
95 terminus which, in our opinion, has not properly been investigated until now. By running MD
96 simulations with a force field specifically designed for intrinsically disordered regions (IDR),
97 we showed that the conformational landscape of the N-terminal peptide is mostly unstructured
98 in solution with almost no helical content. Alternatively, simulation with a standard force field
99 similar to what has been used in previous in silico studies, was found to overstabilize its α-
100 helix content leading to erroneous results. Our findings were confirmed by the ability of the
101 IDR force field to reproduce experimental Cα and Cβ chemical shifts both qualitatively and
102 quantitatively, in contrast to the standard force field.

103 In the second part, we explored the importance of the disordered properties of the N-
104 terminus in the gating mechanism of VDAC. Specifically, experiments by Teijido et al. (14)
105 were modeled by introducing a disulfide bond between residues L10C and A170C. Molecular
106 simulation with the IDR force field at membrane potentials of ±40 mV showed that application
107 of such voltages leads to systematic unfolding of the 3-10 helix involving residues Y7, A8 and
108 D9 and subsequent rearrangement of the unstructured tail of the N-terminus (M1 to T6). At
109 +40 mV (*cis* side), the unfolded portion was found to move further inside the pore leading to
110 steric hindrance of the channel. A metastable state characterized by a low conductance (60%
111 of the conductance in the open state or below) representative of the closed states of VDAC, as
112 well as low anion selectivity or even cation selectivity, was observed. Partial unfolding and
113 repositioning of the N-terminus under applied voltage as well as the inability to induce stable

114 low conducting states with a standard force field suggest that the disordered properties of the
115 N-terminus are critical to account for the closing mechanism of the channel.

116 **2. Results**

117 **2.1 The N-terminal peptide**

118 We first investigated the disordered properties of the N-terminal peptide in solution. Starting
119 from the α-helical N-terminus (M1-G25) directly extracted from the crystal structure of
120 mVDAC1 (9) (PDB ID: 3EMN), we performed μs-long MD simulations using, on one side,
121 the Amber ff14SB force field which is considered one of the standard and latest benchmarks
122 for protein simulations (17) and, on the other side, the ff14IDPSFF force field that was specif-
123 ically designed to sample disordered protein domains (18). Importantly, ff14IDPSFF was re-
124 ported to produce results similar to ff14SB in the case of well-folded systems (18).

125 Representative conformers of the N-terminal peptide obtained after running standard MD
126 with the ff14SB and ff14IDPSFF force fields are shown in Fig 2 (top). Long MD trajectories
127 of 1.6 μs and 2.1 μs were run with ff14SB and ff14IDPSFF, respectively, while convergence
128 was confirmed in both cases as the number of clusters generated from clustering analysis was
129 found to plateau in the last 500 ns (S1 Fig). Notably, important differences in the conforma-
130 tional landscapes of the two force fields were observed. Whereas dynamics performed with
131 ff14SB was mostly characterized by α-helices involving residues Y7 to K20, simulation with
132 the ff14IDPSFF force field led to unstructured conformations including partially as well as
133 fully unfolded structures. To get further insight into the stability of each state, the potential of
134 mean force (PMF) was provided (S2 Fig) as a function of the RMSD with respect to the crystal
135 structure and the radius of gyration (R_g), two popular collective variables for structural analysis
136 of small peptides (19). As depicted in Fig 2 and S2 Fig, transient secondary structures were
137 also identified using ff14IDPSFF including small antiparallel β-strands made of A2-V3 and
138 Y22-G23 (RMSD~11.5Å, R_g~8.5Å) as well as an α-turn involving D9, L10 and G11

(RMSD~9Å, R_g~9Å). The latter was found to minimally contribute to the overall conformational ensemble (1.24%).

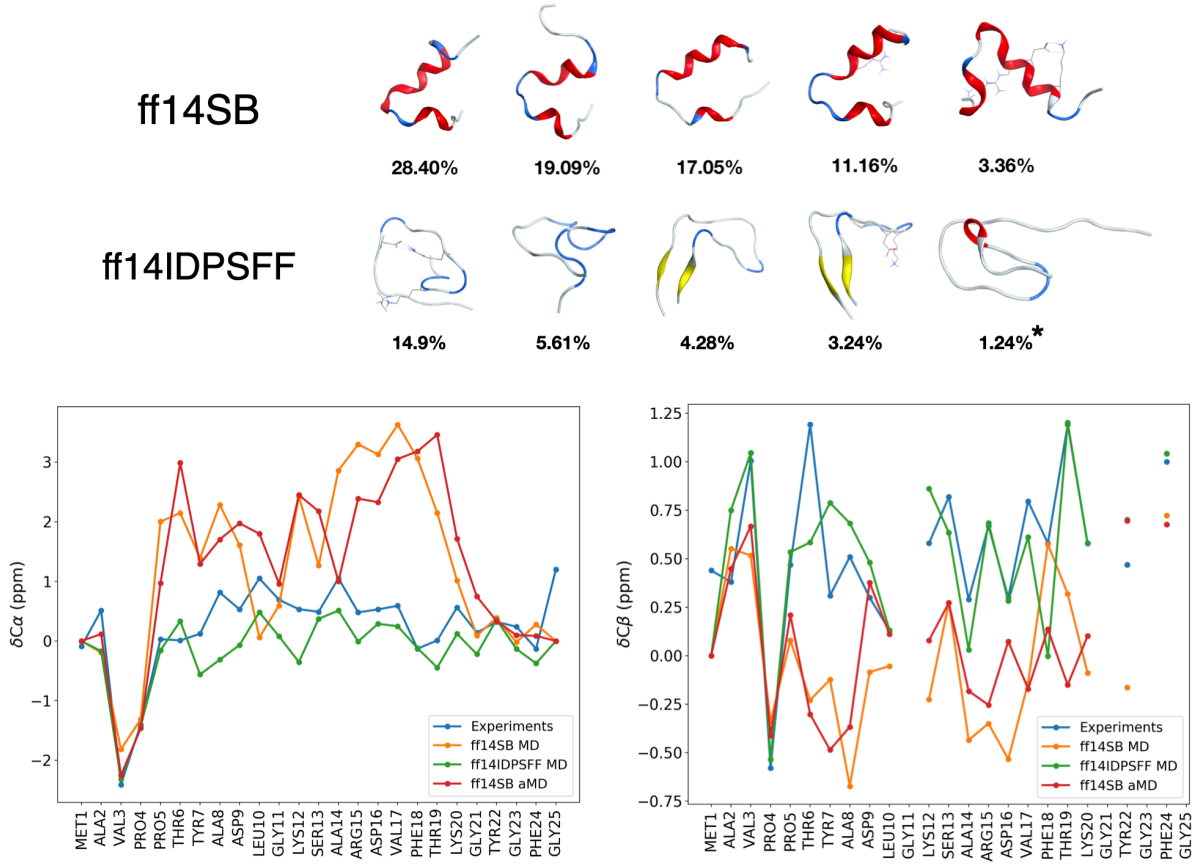

Fig 2. **Representative conformers and chemical shifts of the N-terminal peptide.** Top: representative conformers of the top 5 clusters (and their occupancy) obtained from μs-long simulations with ff14SB and ff14IDPSFF. Note that the last structure (with star) shown for ff14IDPSFF corresponds to the 12th most populated cluster which is the first cluster with α-helical content. Bottom: α- and β-carbons chemical shifts of the N-terminal peptide predicted from molecular simulations and experiments (experimental values were directly extracted from Table S1 in Ref. (16)). Shifts computed from MD simulations were obtained by simple average of the shifts predicted for each generated structure using the SPARTA+ software (20). Shifts computed from aMD simulations were calculated as weighted averages using Maclaurin series up to rank k=10 in order to approximate the weights (Eq. (3)).

Although our simulations were μs-long and convergence was reached in all cases, we explored the possibility that dynamics carried out with ff14SB could produce other

153 conformations of the peptide (over longer timescales) with no α-helical content. To this pur-
154 pose, we used accelerated Molecular Dynamics (aMD), a biasing technique originally devel-
155 oped by the McCammon group (21). aMD has been successfully applied to a vast diversity of
156 systems including the 58-residue pancreatic trypsin inhibitor whereby 500ns-long aMD simu-
157 lation allowed to sample conformations normally reachable on the millisecond timescale (22).
158 Hence, aMD turns out to be a method of choice to investigate the conformational landscape of
159 our 25-residue peptide more thoroughly.

160 Overall, the conformational landscape generated from a 1μs-long aMD simulation with
161 ff14SB was similar to the α-helix ensemble generated from standard MD using the same force
162 field, with no new basin or new structural content reported (S3 Fig). To eliminate the possibility
163 that our simulations could have been biased by our choice of starting structure, i.e., the α-
164 helical N-terminus extracted from mVDAC1, which may have led to the peptide being
165 "trapped" in an α-helix minimum, we also ran a short aMD simulation (20 ns) starting from a
166 fully unfolded structure ($R_g \sim 20$Å). This time was short enough to observe clear convergence
167 to the main α-helix basin found in our long simulation suggesting that further stable or meta-
168 stable regions with ff14SB, were unlikely (S3 Fig).

169 Finally, we investigated the correctness of our results by estimating the NMR chemical
170 shifts of alpha and beta carbons from each simulation and by comparing those values with
171 experimental ones reported elsewhere (16). Results are provided in Fig 2 (bottom) for both
172 ff14SB and ff14IDPSFF force fields where the former is given in cases of standard MD and
173 aMD simulations. Notably, Cα and Cβ chemical shifts predicted using ff14SB were found to
174 be very far from experimental data (chemical shifts obtained from MD and aMD simulations
175 were similar, which is consistent with the similar landscapes observed). Discrepancies were
176 especially visible for α-helix residues confirming the tendency of ff14SB to overexpress sec-
177 ondary structures in disordered systems (23). Conversely, both Cα and Cβ shifts computed

178 from the ff14IDPSFF trajectory showed great agreement with experiments. From S1 Table, we
179 can see that the improvement was both quantitative and qualitative as low RMSE values and
180 high Pearson correlation coefficients (0.870 for Cα and 0.759 for Cβ) were obtained, respec-
181 tively.

182 **2.2 The N-terminus in VDAC**

183 Here we explored the stability of the intrinsically disordered N-terminus as part of the open
184 state of VDAC. MD simulations of mVDAC1 were performed at physiological salt concentra-
185 tion (150 mM KCl) starting from the 3EMN structure (9) embedded in a DOPC/DOPE mem-
186 brane (Fig 1). Since ff14IDPSFF has not yet been tested on proteins interacting with lipids, the
187 new force field parameters were only applied to the N-terminal region which is positioned
188 inside the pore in the open state.

189 As with the N-terminal peptide, standard MD was performed with ff14IDPSFF and com-
190 pared to simulations with the same settings using the ff14SB force field only. In Fig 3, we
191 showed the root mean square fluctuations (RMSF) of N-terminal residues over 100 ns while
192 the inset displays the N-terminal RMSD as a function of time. At first glance, we noticed that
193 both force fields resulted in almost equally-rigid N-terminal regions (RMSD < 2Å) although
194 many residues including L10 to D16 and Y22 to G25 had a slightly higher RMSF in the case
195 of ff14IDPSFF. Interestingly, this increase in flexibility was not necessarily correlated with the
196 ability of secondary structures to unfold. For example, the secondary structure propensity ob-
197 tained with ff14IDPSFF for the long α-helix (residues K12 to T19) was equal or even higher
198 than the propensity calculated with ff14SB (S4 Fig). Alternatively, the 3-10 helix involving
199 Y7, A8 and D9 which is characteristic of the 3EMN structure, was slightly less stable in the
200 case of ff14IDPSFF (0.86 and 0.76 propensity for ff14SB and ff14IDPSFF, respectively).

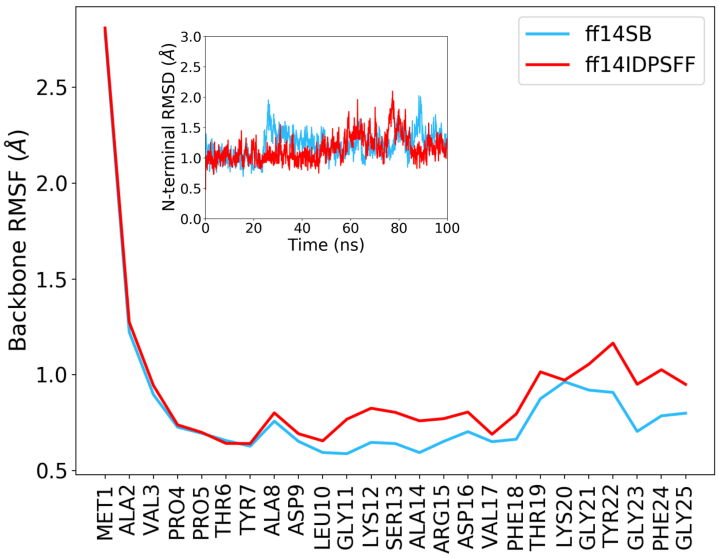

Fig 3. RMSF and RMSD of the N-terminus of wild-type mVDAC1. RMSF and RMSD were computed from 100ns-long runs using ff14SB or ff14IDPSFF. Only the backbone atoms of the N-terminus were considered for the calculation of RMSF. Inset: N-terminal RMSD with respect to the 3EMN structure as a function of time. RMSD values were calculated by first aligning the structures over all the heavy atoms including atoms of the pore and of the N-terminus.

Overall, we found that the ff14IDPSFF force field predicted a stable N-terminal region within the time frame of our standard MD (650 ns) with no apparent transition or change in structural content (especially α-helical one) compared to the 3EMN structure (S1 Video). Not only is this result consistent with experiments showing the stability of the N-terminus in the open state of VDAC (24) but it also confirms the ability of ff14IDPSFF to model stable IDRs as they fold upon interaction with other protein domains.

2.3 Double cysteine mutant

To gain insights into the mechanism triggering closure of VDAC, simulation of a double cysteine mutant (mVDAC1-Cys) characterized by a disulfide bond connecting residues A10C and L170C, was performed. Electrophysiological measurements by Teijido et al. (14) have revealed that this modification was not altering the gating properties of the channel even though the N-

218 terminus was affixed against the barrel. Therefore, such a setup provides a good way to inves-
219 tigate closure of VDAC from molecular simulation as the presence of the S-S bond should
220 dramatically restrict the exploration of the conformational space of the N-terminus, thus saving
221 a lot of computational time. In addition, our results should confirm that closure of the channel
222 is not necessarily induced by large conformational changes of that region.

223 Since our standard MD runs – either with ff14SB or ff14IDPSFF – were unsuccessful in
224 escaping from the basin corresponding to the (S-S bonded) 3EMN structure, aMD simulations
225 were performed. Three membrane potentials: 0 mV, +40mV and −40 mV, at 150 mM KCl,
226 were considered (one aMD trajectory per potential). Voltage was defined as positive when it
227 was greater at the side opposite to the ends of N- and C-termini in the open state. Importantly,
228 this side was found to correlate with the cytosolic side of the channel that was also shown to
229 correspond to the *cis* side in planar lipid bilayer (PLB) experiments (25, 26). Therefore, the
230 potential values specified in the present work most likely represent potential values set at the
231 *cis* side in such experiments while setting the *trans* side to 0 mV.

232 aMD simulations were conducted over hundreds of nanoseconds at each voltage (char-
233 acteristics of all our simulations, including simulation times, are provided in S2 Table). While
234 trajectories generated with ff14SB did not reveal any major displacements of the N-terminus
235 or changes in its secondary structure at all applied potentials (S2 Video), simulations with
236 ff14IDPSFF showed different induced mechanisms depending on the voltage. aMD trajectories
237 at +40 mV and −40 mV were both characterized by early unfolding of the 3-10 helix involv-
238 ing residues Y7, A8 and D9 (after 20 ns at +40 mV and after 2 ns at -40 mV). At 0 mV, the
239 3-10 helix was more stable although our aMD trajectory also led to unfolding of this region
240 after 160 ns (S3 Video) suggesting that such an event is not fully induced by the membrane
241 potential. Analysis of representative frames in that case indicated that unfolded residues Y7,
242 A8 and D9, initially interacting with the β-barrel at strands 8 and 9 could establish contacts

with residues of strands 6 to 7, e.g., via hydrogen bonds at Y7-T98 or A8-N124 (S5 Fig). Despite unfolding of the 3-10 helix, position and orientation of the N-terminus including those of the N-terminal tail (M1 to T6) remained globally unchanged at 0 mV as evidenced by hydrogen bonds at M1-E121, A2-H122 or P4-N124 prevailing all along our simulation.

Contrary to the 0 mV case, our +40 mV aMD trajectory showed a significant shift of the N-terminal tail whereby residues M1 to P5 moved further inside the barrel around 140 ns (Fig 4, S4 Video). Closer look at molecular surfaces revealed that the presence of the N-terminus in this region sterically reduced the opening of the channel. Once inside the pore, the tail was found to either interact with the β-barrel at strands 4 and 5 (hydrogen bonds at M1-E84, A2-E84), detach from it or interact with other residues of the N-terminus (hydrogen bonds at M1-D9 and A2-Y7) indicative of a high flexibility of that region. At −40 mV, we noticed that the N-terminal tail converged in a more "packed-up" conformation (S5 Video). Although residue M1 was found to interact electrostatically with E121 just as in the 0 mV case, hydrogen bonds and hydrophobic patch between residues T6, Y7, A8 and strands 7 and 8 were also reported, which occasionally led to slight compression of the barrel and further obstruction of the channel opening in the region of interaction (Fig 4, S6 Fig (cluster 5) and S7 Fig).

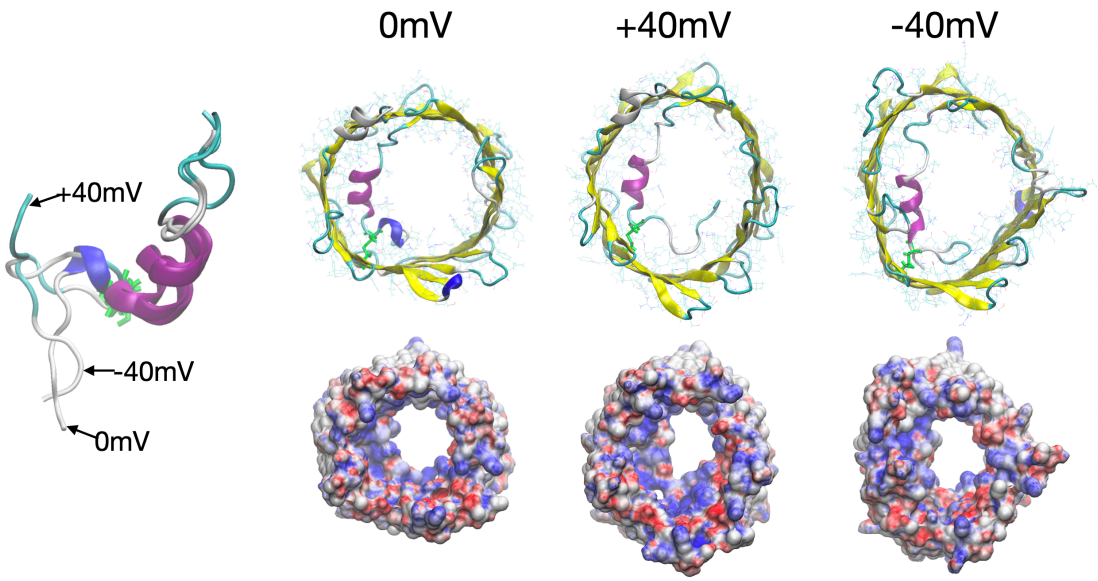

Fig 4. Open and subconducting conformations of mVDCA1-Cys. Left: specific arrangements of the N-terminus (lateral view) obtained at different voltages with ff14IDPSFF. Conformations at +40 mV and -40mV correspond to states with a low conductance (50–60% of the conductance in the open state) and a slight cation selectivity, while the conformation at 0 mV represents the 3EMN structure after a 10-ns equilibration. The A10C-L170C disulfide bond is depicted in green. Right: cytosolic view of mVDAC1-Cys structures associated with the N-terminal conformers displayed on the left. Top structures correspond to ribbon representations whereas bottom ones represent electrostatic surfaces (red and blue colors stand for negative and positive potentials, respectively, ranging between −10.0 and 10.0 (values in kT/e)).

To investigate whether any of the conformations generated from aMD could correspond to closed states of VDAC, we performed grand canonical Monte Carlo/Brownian dynamics (GCMC/BD) which enable to rapidly simulate the flow of ions across membrane channels (27) GCMC/BD has been successfully applied to porin systems (28) including the open state of VDAC (29). In GCMC/BD, only ions are explicitly simulated while the rest of the system including the protein and the membrane, is modeled as a fixed continuous dielectric. In the present study, clustering analysis was carried out on each aMD trajectory (0 mV, +40 mV and −40 mV) by generating 500 clusters in each case. Next, independent GCMC/BD trajectories were run at 150 mM KCl from the representative structure of each cluster to approximate the

277 conductance and anion/cation ratio of each state. Estimates were obtained by running
278 GCMC/BD at a single voltage value for each frame (at +40 mV for frames generated at
279 +40 mV and 0 mV, and at −40 mV for frames extracted from the −40 mV trajectory).

280 From this approach, we observed that the conductance of the channel remained globally
281 stable at 0 mV with an average value of 0.918 nS and few conformations below 0.6 nS (S8
282 Fig). Importantly, this mean value is relatively close to the experimental conductance value of
283 the open state given at 0.81 nS at 150 mM KCl concentration (6). As another remark, no visible
284 change in the conductance was reported upon unfolding of the 3-10 helix (160 ns) confirming
285 that the channel was still in its open state after such an event. Regarding the anion/cation ratio,
286 experiments have estimated it to be around 5 in the open state of the wild-type VDAC1 at 150
287 mM KCl (6). In our simulation, large fluctuations of this ratio, characterized by high values
288 (> 40) and an average value of 14, were reported. We speculate that such high ratios are due
289 to the small number of cations crossing the pore during our GCMC/BD runs (often less than
290 5), which are expected to lead to an overestimation of the anion selectivity in the open state.

291 At +40 mV, our GCBC/BD runs revealed a drop in the conductance at about 250 ns in
292 our aMD simulation with many structures below 0.6 nS (Fig 5), where 0.6 nS corresponds to
293 65.3% of the conductance measured at 0 mV. At this stage, the channel was characterized by
294 a zigzag N-terminal tail located midway inside the pore and interacting with the β-barrel
295 through hydrophobic interactions as well as hydrogen bonds between E84 and the very end of
296 the N-terminus (M1, A2, V3; S7 Fig). The drop in the conductance was coupled by a significant
297 decrease in the anion/cation ratio with values around 3 or below as well as a few structures
298 exhibiting slight cation selectivity. From 280 ns, conductance slowly increased again which
299 happened when the tail detached again from the barrel.

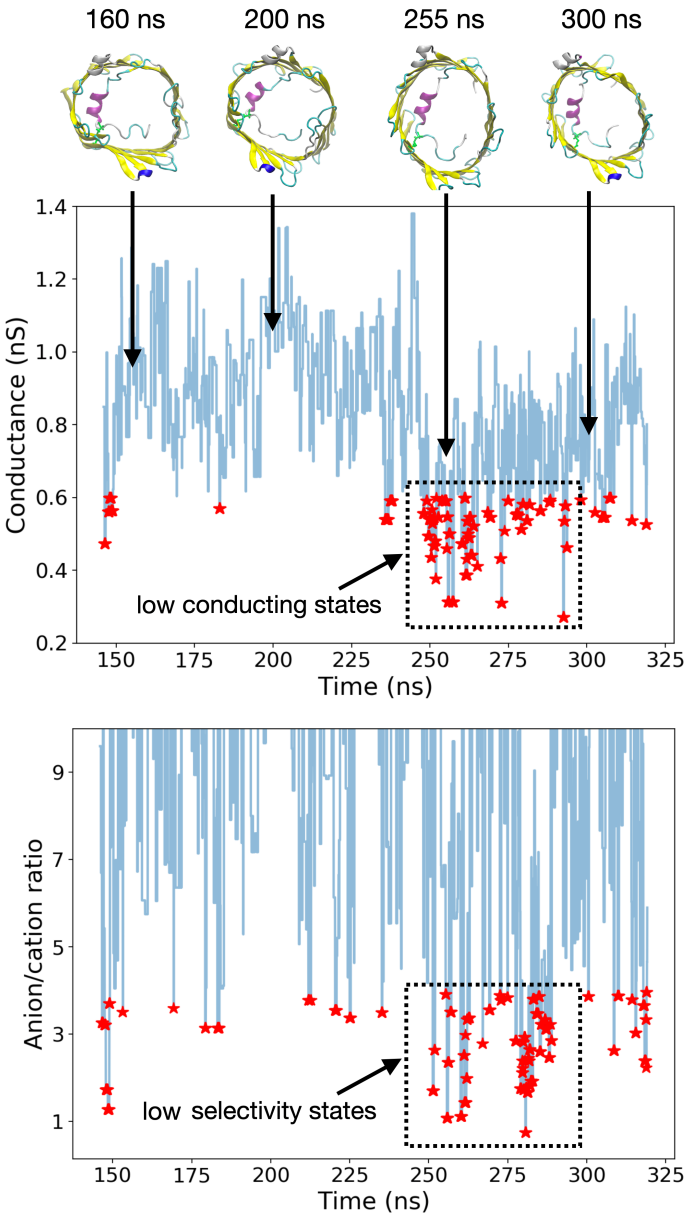

Fig 5. Conductance and anion/cation ratio of mVDAC1-Cys structures generated at +40mV. All values were estimated from GCMC/BD simulations at +40mV (150 mM KCl) performed on 500 representative structures of our +40mV aMD trajectory (once the N-terminal tail has detached and moved inside the barrel (~140 ns)). Time curves were reconstructed by assigning the same conductance and anion/cation ratio to all the frames of a given cluster. Red stars correspond to all the frames with a conductance less than 0.6 nS or an anion/cation ratio less than 4.

Unlike the +40 mV case, our GCBC/BD simulations performed on our −40 mV aMD trajectory did not show any long-lived subconducting state (S8 Fig). Nevertheless, a few

transient conformations characterized by both a low conductance and reduced anion selectivity or even cation selectivity, were found, especially when the packed N-terminal tail interacted with the barrel leading to slight compression of the latter in the region of interaction (Fig 4 (−40 mV) and S7 Fig). In Fig 6, we reported the results obtained from GCMC/BD runs at different voltages for the low conducting conformations identified at +40 mV and −40 mV which are characterized by slight cation selectivity. The tested frames correspond to those depicted in Fig 4. As a comparison, we also provided the results of mVDAC1-Cys equilibrated from the 3EMN crystal structure at 0 mV which is expected to be representative of the open state of the channel. Conductances, i.e., slopes of the I/V curves, were found to be 1.01 nS, 0.45 nS and 0.58 nS for structures generated at 0 mV, +40 mV and −40 mV, respectively, while mean anion/cation ratios (averaged over all voltages) were estimated at 5.96, 1.10 and 0.92.

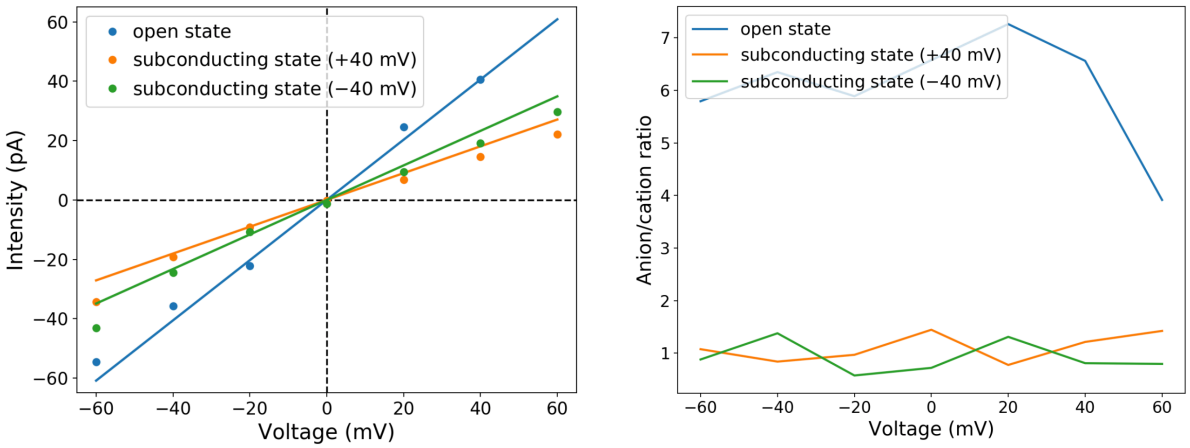

Fig 6. Intensity and anion/cation ratio of open and subconducting conformations of mVDAC1-Cys as a function of voltage. Tested conformations correspond to the ones displayed in Fig 4. Left: I/V curves. The slopes correspond to the conductance (values in nS) estimated at 1.01, 0.45 and 0.58 for the structures generated at 0 mV, +40 mV and -40 mV, respectively. Right: predicted anion/cation ratio; mean values (averaged over all voltages) were found to be 5.96, 1.10 and 0.92, respectively.

329 ## 3. Discussion

330 In the present study, the intrinsically disordered nature of the N-terminus of VDAC as well as
331 its importance in the gating mechanism of the channel were explored. Although not fully
332 acknowledged until now, several arguments in favor of an intrinsically disordered N-terminal
333 segment in VDAC can be put forward: (i) using NMR and CD techniques, De Pinto and
334 coworkers have shown that a free peptide corresponding to such a domain mostly exists as a
335 random coil in solution (15, 16). As the N-terminus of VDAC is known to translocate out of
336 the pore of the channel in specific environmental conditions (12), it was suggested that these
337 unstructured properties were essential in the interaction of VDAC with other proteins (16); (ii)
338 closer look at the sequence of the N-terminal domain reveals that 13 (out of 25) residues belong
339 to the well-known eight disordered-promoting residues, namely, G, A, S, P, R, Q, E and K.
340 Such residues were originally identified from analysis of various X-ray, NMR and CD data, as
341 being more prevalent in disordered segments (30). In VDAC, disordered-promoting residues
342 specifically include A8, G11, K12, S13, A14 and R15, six amino acids involved in the α-helix
343 domain of the N-terminus in the open state; (iii) application of disorder-prediction software
344 like ESpritz (31) which relies on bidirectional recursive neural networks, predicted that all
345 residues of the N-terminus were disordered (not shown). We noticed that this result was inde-
346 pendent of the choice of the training set (X-ray or DisProt) used by the ESpritz program (31);
347 (iv) a feature of many disordered systems is that they can fold into different structures when
348 binding to other proteins or protein domains (32). Interfaces which are crucial to stabilize sec-
349 ondary structures were reported to be significantly more hydrophobic than those of globular
350 protein complexes (33). In the open state of VDAC, the vast majority of interactions between
351 the helical N-terminus and the β-barrel are non-polar (9). These include the well-known hy-
352 drophobic patch between L10 and V143-L150 that was shown to be highly conserved across
353 species (8, 9).

354 Along with the above arguments, further evidence of the disordered properties of the N-
355 terminus of VDAC was provided in the present work where MD performed with the IDR-
356 specific ff14IDPSFF force field enabled to reproduce experimental chemical shifts of the free
357 N-terminal peptide while the standard ff14SB force field was unsuccessful in doing so. From
358 a structural point of view, simulations with ff14SB were characterized by a significant amount
359 of α-helical content that was most likely responsible for the large deviation from experimental
360 values. Importantly, the tendency of popular force fields to overstabilize secondary structures
361 in disordered systems is not new and is due to force field parameters, especially dihedral cor-
362 rection terms, which are normally calibrated from databases of well-folded proteins (34-36).
363 Such force fields include ff14SB, CHARMM27 and ff99SB which have been extensively used
364 in previous in silico studies on VDAC (16, 37-39). Conversely, our simulation with the IDR-
365 specific force field showed almost no α-helical content in the free peptide aside from a small
366 α-turn made of D9, L10 and G11. The complete absence of an α-helical segment similar to the
367 one observed in the crystal structures of VDAC indicates that the α-helix pattern characteristic
368 of the open state is formed via induced folding through interaction with the β-barrel and not
369 via conformational selection as previously presumed (16). Moreover, the ability of ff14IDPSFF
370 to properly simulate well-folded systems was confirmed by our MD simulations of mVDAC1
371 in its open state whereby the N-terminus remained stable all along a 650ns-long trajectory.
372 In the second part, we investigated whether the disordered properties of the N-terminus
373 were of importance for the gating mechanism of VDAC. This was done by running aMD sim-
374 ulations of a double cysteine mutant (mVDAC1-Cys) made of a disulfide bridge connecting
375 residues A10C and L170C. As shown by Teijido et al. (14), such an experiment enabled to
376 induce closed states of the channel while affixing part of the N-terminus against the barrel, thus
377 restricting the exploration of the conformational landscape. Just like the free peptide, striking
378 differences between the ff14SB and ff14IDPSFF force fields were noticed. Whereas the N-

379 terminus of VDAC with ff14SB was insensitive to a +40 mV voltage (no conformational or
380 structural change observed), simulation with ff14IDPSFF at the same voltage showed that the
381 N-terminal tail (M1 to T6) could detach from the β-barrel subsequent to unfolding of the 3-10
382 helix (Y7, A8 and D9). The tail was found to move further inside the pore while the long α-
383 helix (K12 to T19) remained folded and stable interacting with the barrel all along our simula-
384 tion. Using GCMC/BD simulations performed on representative structures, we managed to
385 identify a large number of conformations characterized by a low conductance (~60% of the
386 conductance measured in the open state or below). As a comparison, the conductance in the
387 closed states was experimentally estimated at 50% of the conductance in the open state (5, 6)
388 but could well vary between 40% and 70% (13, 39), which is consistent with the values ob-
389 tained here. At the same time, electrophysiological experiments have revealed that closed states
390 of the wild-type VDAC1 were cation selective (5,6). Although our subconducting states were
391 associated with a low anion/cation ratio (3 or below), few generated frames were found to be
392 cation selective. This result can be due to the presence of the disulfide bridge that prevents
393 further rearrangement of the N-terminus required for a full cation selectivity (40). For the rec-
394 ord, mVDAC1-Cys was experimentally found to exhibit typical gating profile in terms of con-
395 ductance (14), yet no measurement of the anion/cation ratio has been reported that could con-
396 firm cation preference of the closed states in that case.

397 Our inability to induce significant displacement of the N-terminus at +40 mV with a
398 standard force field is consistent with previous MD studies based on CHARMM force fields,
399 which led to the same conclusion (38, 39). In Ref. (39), membrane potential as high as 400 mV
400 could only generate transient subconducting states of the wild-type VDAC1. It was proposed
401 that this result was due to the limitation of standard MD to simulate systems beyond the μs
402 timescale. However, our success in generating a metastable subconducting state at +40 mV
403 with an IDR-specific force field – where 40 mV is a typical voltage at which closure is

404 normally detected – raises the question of the efficiency of popular force fields to properly
405 account for the gating mechanism. As the unstructured N-terminal tail was found to relocate
406 inside the pore after unfolding of the 3-10 helix, disordered properties of the N-terminus appear
407 to be essential to induce long-lived closed states. As another remark, no apparent increase in
408 the ellipticity of the barrel was reported during the formation of our subconducting states
409 indicating that closure of VDAC is not necessarily correlated with semicollapsed states as
410 previously suggested (11).

411 Finally, our simulations at −40 mV only revealed transient subconducting states, which,
412 due to their unstability, may not fully represent the experimental closed states observed at this
413 voltage. Nevertheless, our low conducting conformations characterized by a rearrangment of
414 the unstructured N-terminal tail in a direction opposite to the +40 mV tail (Fig 4) combined
415 with a slight deformation of the barrel due to its interaction with the N-terminus, suggest that
416 a different structural mechanism is involved in the formation of closed states at negative
417 potential. More thorough studies, e.g., via longer simulations or the use of other MD biasing
418 techniques, are required to get a full picture of the closing mechanism of the channel in that
419 case.

420

421 **4. Material and Methods**

422 **4.1 MD software and force fields**

423 All our MD simulations, including standard and aMD simulations, were performed using the
424 Amber16 package (41). The ff14SB force field (17). which is known as the latest Amber force
425 field benchmark for proteins simulations is directly available from the Amber package while
426 the ff14IDPSFF force field (18) was obtained from direct request to Prof. Ray Luo's group.
427 ff14IDPSFF can also be downloaded from the Precise Force Field and Bioinformatics Labor-
428 atory website: http://cbb.sjtu.edu.cn/~hfchen/index_en.php.

429 **4.2 Structure preparation (peptide)**

430 The N-terminal peptide was obtained by extracting the N-terminal region (M1-G25) from the
431 mVDAC1 structure in the open state (PDB ID: 3EMN (9)). Protonation of the peptide was
432 done using the PropKa algorithm from the MOE 2018 software at a neutral pH (42). Using the
433 Amber's LEaP module, the system was set into an octahedral box filled with TIP3P waters
434 requesting at least a 15Å distance between any atom of the peptide and the box edges. Overall,
435 8826 water molecules were incorporated into the simulation box. Sodium and chloride ions
436 were added to neutralize the system as well as to approximate a 0.01M concentration consistent
437 with experimental conditions used for NMR chemical shifts measurements (16). Both ff14SB
438 and ff14IDPSFF simulations of the N-terminal peptide were based on the above preparation
439 protocol. However, setting up ff14IDPSFF simulations further required to generate a new to-
440 pology file containing the proper force field parameters (dihedral correction terms). This was
441 done by running the Trans_FF_IDPs.pl script available with the ff14IDPSFF force field using,
442 as an input, the ff14SB topology file generated from the LEaP module (41). For each force
443 field, equilibration of the solvated structure was performed with the Amber's pmemd utility by
444 first minimizing the whole system (peptide and solvent) during 5000 steps using the steepest
445 descent method followed by 5000 steps of conjugate gradient. Next, simulations in the NVT
446 ensemble were carried out for 500 ps by slowly heating the system from 0K to 298K while
447 restraining heavy atoms of the peptide. Lastly, NPT simulations at $P = 1$ bar and $T = 298$K
448 were run without restraints during 500 ps to finalize the equilibration process.

449 **4.3 MD production (peptide)**

450 Unbiased MD production was conducted during 1.6 μs and 2.1 μs using the ff14SB and
451 ff14IDPSFF force field, respectively. aMD simulations performed with the ff14SB force field
452 were run during 1 μs. Details regarding the aMD method and our protocol are given below.
453 Additional aMD simulations starting from a fully unfolded structure of the peptide were run

454 using the ff14SB force field during 20 ns, which was found to be enough to reach the α-helix
455 basin. In that case, the initial conformation was simply extracted from our ff14IDPSFF simu-
456 lation by selecting the structure with maximum radius of gyration (≥ 20Å).

457 **4.4 Accelerated MD**

458 To efficiently sample the conformational space of the N-terminal peptide and of mVDAC1-
459 Cys, aMD simulations were run. Briefly, aMD is based on adding a non-negative biasing po-
460 tential (boost) to the system whenever the system potential is lower than an energy threshold
461 (43):

$$V'(\boldsymbol{x}) = V(\boldsymbol{x}) \quad \text{when } V(\boldsymbol{x}) \geq E$$
$$V'(\boldsymbol{x}) = V(\boldsymbol{x}) + \Delta V(\boldsymbol{x}) \text{ when } V(\boldsymbol{x}) < E, \tag{1}$$

462 where $V(\boldsymbol{x})$ is the true MD potential, $\Delta V(\boldsymbol{x})$ is the aMD boost and E is the energy threshold.
463 The addition of the $\Delta V(\boldsymbol{x})$ term is done in such a way as to reduce the height of local energy
464 barriers, and is therefore dependent on the energy of the system at $\boldsymbol{x}$. In the present work, aMD
465 was run in its dual boost version, i.e., the aMD boost is the sum of two biasing contributions:
466 one acting on all atoms (including solvent atoms) through the total potential energy $V(\boldsymbol{x})$, and
467 the other one acting only on dihedral angles through the dihedral energy $V_d(\boldsymbol{x})$ such that:

$$\Delta V(\boldsymbol{x}) = \frac{(E_p - V(\boldsymbol{x}))^2}{\alpha_p + E_p - V(\boldsymbol{x})} + \frac{(E_d - V_d(\boldsymbol{x}))^2}{\alpha_d + E_d - V_d(\boldsymbol{x})} \tag{2}$$

468 Here E_p and E_d correspond to the average (total) potential and dihedral energies of the biased
469 simulations, respectively, whereas α_p and α_d are coefficients accounting for the contribution
470 of each biasing term. Following standard aMD protocols (22, 44), the above coefficients were
471 computed from the following formulas:

$$E_p = E_{p,0} + \gamma_p \cdot n_{atoms}, \qquad \alpha_p = \gamma_p \cdot n_{atoms}$$

$$E_d = E_{d,0} + \gamma_d \cdot n_{residues} + \gamma_d' \cdot n_{lipids}, \qquad \alpha_d = 0.2\left(\gamma_d \cdot n_{residues} + \gamma_d' \cdot n_{lipids}\right),$$

where $\gamma_p = 0.16$ kcal/mol/atom, $\gamma_d = 3.5$ kcal/mol/residue and $\gamma_d' = 30.0$ kcal/mol/lipid. n_{atoms}, $n_{residues}$ and n_{lipids} are the number of atoms (including solvent atoms), the number of residues (25 in the case of the peptide) and the number of lipids, respectively. $E_{p,0}$ and $E_{d,0}$ are the average potential and dihedral energies of the unbiased system, respectively, which were estimated from direct analysis of our equilibration simulations in the NPT ensemble (see above).

4.5 aMD reweighting

An important feature of aMD is the possibility to recover ensemble averages associated with the true MD profile. As is well known, structures generated from a biased (equilibrated) simulation characterized by a biasing potential $\Delta V(\boldsymbol{x})$ can be assigned a weight $\mathrm{w}(\boldsymbol{x})$ accounting for how they really contribute to the unbiased free energy. This weight is given by the Boltzmann factor: $\mathrm{w}(\boldsymbol{x}) = e^{\Delta V(\boldsymbol{x})/k_b T}$ that enables to compute the average of any collective variable $\xi(\boldsymbol{x})$ as

$$\langle \xi \rangle = \frac{1}{\sum_i \mathrm{w}(\boldsymbol{x}_i)} \sum_i \mathrm{w}(\boldsymbol{x}_i)\xi(\boldsymbol{x}_i) \tag{3}$$

where $\boldsymbol{x}_i$ are the coordinates of the structures generated through the biased simulation. Notably, the exponential factors can be expressed as a Maclaurin series (45) such that:

$$\mathrm{w}(\boldsymbol{x}) = \sum_{k=0}^{\infty} \frac{1}{k!} (\Delta V(\boldsymbol{x})/k_b T)^k \tag{4}$$

In practice, finite sampling leads to small errors in the distribution of the $\Delta V(\boldsymbol{x_i})$ while high-order terms in the above series contribute to increase that noise. Therefore, it is of

common practice to approximate the weights $\mathrm{w}(\boldsymbol{x})$ by keeping only low-order terms. In this work, all averages quantities deduced from our aMD simulations, including chemical shift estimations, were computed from Eqs. (3) and (4) by keeping only terms up to $k = 10$. Although widely accepted, we have tested the applicability of the mentioned formulas on a toy model – alanine dipeptide in explicit solvent – by confirming that averages of φ, ψ dihedral angles of the peptide from aMD data could well reproduce averages obtained from standard MD (not shown).

4.6 Chemical shifts

Cα and Cβ chemical shifts were calculated using the SPARTA+ software (20) which relies on a neural network algorithm to predict the shifts from an input protein structure. The high execution speed of the program enabled to compute the chemical shifts for each structure saved throughout our MD or aMD simulations (one structure saved every 2 ns). Standard averages of each chemical shift – or weighted averages in the case of aMD data – were computed from those predictions and directly compared with experimental data (Table S1 in Ref. (16)).

4.7 Structure preparation (channel)

Structures of mVDAC1 and mVDAC1-Cys were prepared from the 3EMN crystal structure by aligning the protein to its corresponding *Orientation of Protein in Membranes* (OPM) structure (46). This enabled to translate the system so that its center of mass was positioned at the origin and the pore was oriented along the z axis. In the case of mVDAC1-Cys, the MOE program (42) was used to mutate residues L10 and A170 into cysteines and to create the disulfide bond. The channel was then embedded into a DOPC/DOPE membrane using the CHARMM-GUI membrane builder webserver (47). A rectangular simulation box with TIP3P water was considered. The membrane was built following a 2:1 PC:PE ratio as it was shown to be representative of the lipid composition of the MOM (48). Lipids were positioned in such a way as to approximatively cover a 90 x 90 $Å^2$ surface in x and y directions which resulted in 186 lipid

514 molecules. Thickness of water layers on both sides of the membrane was set to 22.5 Å creating
515 around 12500 water molecules in the box. Protonation of protein residues was performed with
516 the membrane builder tool. As suggested in Ref. (39), the E73 residue was kept in its unproto-
517 nated form although it was initially facing the membrane. A 150 mM-KCl concentration was
518 applied in all our simulations. Finally, equilibration protocol involving minimization, NVT and
519 NPT steps, was similar to the one used for the free peptide except NPT equilibration was run
520 during 5ns (mVDAC1) or 10ns (mVDAC1-Cys) using an anisotropic pressure scaling as is
521 required for membrane systems. See the section "structure preparation (peptide)" for other pa-
522 rameter values.

523 **4.8 Production (channel)**

524 Production runs of wild-type mVDAC1 were performed in the NPT ensemble while those re-
525 lated to mVDAC1-Cys were conducted in NVT starting from structures equilibrated in NPT.
526 A summary of our simulations including simulation lengths is provided in S2 Table. Membrane
527 potentials were modeled by introducing an external electric field along the z-axis using Am-
528 ber's "efz" parameter. Voltages include 0 mV, +40 mV and −40 mV. The reason for running
529 production in NVT was due to the inability of the Amber package to account for virial contri-
530 bution in NPT upon application of an external field.

531 **4.9 GCMC/BD**

532 Poisson-Boltzmann and Poisson-Nernst-Planck (PB/PNP) and GCMC/BD calculations were
533 run using the open-source PB/PNP and GCMC/BD programs available at http://www.charmm-
534 gui.org/?doc=input/gcmcbd. For more details about the PB/PNP and GCMC/BD protocols, see
535 Refs. (27, 49). GCMC/BD simulations were carried out on representative frames of our aMD
536 trajectories of mVDAC1-Cys at 0 mV, +40 mV and −40 mV. RMSD clustering analysis was
537 performed from the full trajectory generated at 0 mV, from 140 ns at +40 mV, i.e., when the
538 N-terminal tail has moved inside the barrel, and from 300 ns at −40 mV. In all cases, 500

539 clusters resulting in 500 frames were generated. Next, the CHARMM-GUI GCMC/BD Ion
540 Simulator webserver (50) was used to generate all the input files needed for PB/PNP and
541 GCMC/BD calculations. Each structure was embedded into a 35Å-thick membrane oriented
542 along the z-axis and positioned in the middle of an 85 x 85 x 95 $Å^3$ box with a grid spacing of
543 0.5Å. Thickness of buffer regions at the top and bottom of the simulation box were set to 5Å
544 while a fixed concentration of 150-mM KCl was used on both sides of the membrane. Each
545 GCMC/BD simulation was done by performing one GCMC step every BD step for a total of
546 5.10^7 BD cycles. Values reported in Fig 5 and S8 Fig were obtained from averaging over 3
547 independent GCMC/BD replicas. The transmembrane voltage was set to $+40$ mV for frames
548 extracted from 0 mV- and $+40$ mV aMD trajectories and to -40 mV for frames extracted from
549 the -40 mV aMD trajectory. Conductance was estimated by summing up K+ and Cl- currents
550 and dividing by the applied voltage. Anion/cation ratio was computed as the ratio of the Cl-
551 flux to the K+ flux. Finally, values reported in Fig 6 were obtained from averaging over 10
552 replicas at each specified voltage.
553

554 **Supporting information**

555 **S1 Fig. Convergence of standard MD simulations of the N-terminal peptide.** The figure
556 shows the number of clusters generated as a function of the simulation time in the case of the
557 ff14SB force field (a) and of the ff14IDPSFF force field (b). Clustering analysis was performed
558 using a hierarchical agglomerative approach with an RMSD threshold of 3Å.

559 **S2 Fig. PMF profiles generated from standard MD simulations of the N-terminal peptide.**
560 PMFs were obtained in the cases of ff14SB (top) and of ff14IDPSFF (bottom) and are given
561 as a function of the radius of gyration (R_g) and of the RMSD with respect to the N-terminal
562 conformation in the crystal structure of mVDAC1. Representative structures in main basins

563 and transition regions are also depicted. The top figure was built out of a 1.6 μs-long trajectory
564 while data at the bottom were collected over 2.1 μs.

565 **S3 Fig. PMF profile generated from aMD simulation of the N-terminal peptide with the**
566 **ff14SB force field.** Due the biased nature of the simulation, density values were reweighted
567 from a Maclaurin series up using terms up to rank $k = 10$ (Eq. (4)). As in S2 Fig, the PMF is
568 given as a function of the radius of gyration (R_g) and the RMSD with respect to the N-terminal
569 conformation in the crystal structure of mVDAC1. The dashed dark-blue trajectory represents
570 a 20ns-long aMD trajectory generated by initiating our simulation from a fully unfolded
571 structure (dark blue cross) that clearly shows the convergence to the helix-enriched basin.

572 **S4 Fig. Secondary structure content of wild-type mVDAC1.** Values were obtained from
573 100ns-long MD runs using the ff14SB force field (left) and the ff14IDPSFF force field (right).
574 Note that β-content is not displayed as it is everywhere zero and helical content includes both
575 3-10 and regular alpha-helix content. For both force fields, 3-10 content is found only in the
576 short helix made of residues TYR7 to ASP9 and regular alpha content was only observed in
577 the long helix made of residues LYS12 to THR19.

578 **S5 Fig. Representative conformers of mVDAC1-Cys (and their occupancy) at 0 mV.** Con-
579 formers were extracted from a 540ns-long aMD trajectory generated with the ff14IDPSFF
580 force field. The A10C-L170C disulfide bond is depicted in green. Hydrogen bonds involving
581 residues of the end of the N-terminus (especially residues Y7, A8 and D9) and residues of the
582 β-barrel are shown in pink.

583 **S6 Fig. Representative conformers of mVDAC1-Cys (and their occupancy) at -40 mV.**
584 Conformers were extracted from a 630ns-long aMD trajectory generated with the ff14IDPSFF
585 force field. The A10C-L170C disulfide bond is depicted in green. Hydrogen bonds involving
586 residues of the end of the N-terminus (especially residues Y7, A8 and D9) and residues of the

β-barrel are shown in pink. The two last conformers exhibit visible deformation of the barrel in the region of interaction.

S7 Fig. Contact maps of low conducting conformations of mVDAC1-Cys. Conformations correspond to the ones displayed in Fig 4 at +40 mV (left) and -40 mV (right).

S8 Fig. Conductance and anion/cation ratio of mVDAC1-Cys structures generated at 0mV, +40 mV and -40mV. All values were obtained from GCMC/BD runs at 150 mM KCl concentration performed on 500 representative structures of each aMD trajectory. Time curves were reconstructed by assigning the same conductance and anion/cation ratio to all the frames of a given cluster. Red stars correspond to all the frames with a conductance less than 0.6 nS or an anion/cation ratio less than 4. Note that the frames extracted from our aMD trajectories at +40mV and -40mV were selected from 140 ns and 300 ns, respectively.

S1 Table. RMSE and Pearson correlation coefficient (R) obtained by comparing experimental and simulated chemical shifts of the N-terminal peptide. Simulations include MD and aMD ones using either the ff14SB or the ff14IDPSFF force field.

S2 Table. Characteristics of molecular simulations of mVDAC1 (wild-type and double Cys mutant) performed in the current study.

S1 Video. Clip of the MD trajectory of wild-type mVDAC1 (650 ns) with the ff14IDPSFF force field in the absence of applied voltage. No conformational transition or change in secondary structure content was observed.

S2 Video. aMD trajectory of mVDAC1-Cys (420 ns) at +40mV with the ff14SB force field. The A10C-L170C disulfide bond is shown in green. No conformational transition or change in secondary structure content was observed.

611 **S3 Video. aMD trajectory of mVDAC1-Cys (540 ns) at 0mV with the ff14IDPSFF force**
612 **field.** The A10C-L170C disulfide bond is shown in green. The 3-10 helix made of residues Y7,
613 A8 and D9 was found to unfold at 160 ns. However, the position of the N-terminal tail (M1-
614 P5) and of the long-helix (K12 to T19) remained unchanged.

615 **S4 Video. aMD trajectory of mVDAC1-Cys (320 ns) at +40mV with the ff14IDPSFF force**
616 **field.** The A10C-L170C disulfide bond is shown in green. The 3-10 helix made of residues Y7,
617 A8 and D9 was found to unfold at 20 ns. Subsequently, the N-terminal tail (M1-P5) moves
618 further inside the barrel (at 140 ns) leading to steric hindrance of the pore.

619 **S5 Video. aMD trajectory of mVDAC1-Cys (630 ns) at -40mV with the ff14IDPSFF force**
620 **field.** The A10C-L170C disulfide bond is shown in green. The 3-10 helix made of residues Y7,
621 A8 and D9 was found to unfold at 2 ns.

622

623 **Author Contributions**

624 Conceptualization: Jordane Preto, Isabelle Krimm
625 Formal analysis: Jordane Preto
626 Investigation: Jordane Preto
627 Methodology: Jordane Preto, Isabelle Krimm
628 Resources: Isabelle Krimm
629 Software: Jordane Preto
630 Supervision: Isabelle Krimm
631 Visualization: Jordane Preto
632 Writing – original draft: Jordane Preto, Isabelle Krimm
633 Writing – review & editing: Jordane Preto, Isabelle Krimm

634

Acknowledgments. We gratefully acknowledge support from the PSMN (Pôle Scientifique de Modélisation Numérique) of the ENS de Lyon for the computing resources.

Competing interests. The authors have declared that no competing interests exist.

References

(1) Shoshan-Barmatz V, De Pinto V, Zweckstetter M, Raviv Z, Keinan N, Arbel N. VDAC, a multi-functional mitochondrial protein regulating cell life and death. Mol Aspects Med 2010 June 01;31(3):227-285.

(2) Shoshan-Barmatz V, Maldonado EN, Krelin Y. VDAC1 at the crossroads of cell metabolism, apoptosis and cell stress. Cell Stress 2017 October 01;1(1):11-36.

(3) Magri A, Reina S, De Pinto V. VDAC1 as Pharmacological Target in Cancer and Neurodegeneration: Focus on Its Role in Apoptosis. Front Chem 2018 April 06;6:108.

(4) Bergdoll L, Grabe M, Abramson J. An Assessment of How VDAC Structures Have Impacted Our Understanding of Their Function. Molecular Basis for Mitochondrial Signaling: Springer; 2017. p. 141-160.

(5) Colombini M. VDAC structure, selectivity, and dynamics. Biochim Biophys Acta 2012 June 01;1818(6):1457-1465.

(6) Hodge T, Colombini M. Regulation of metabolite flux through voltage-gating of VDAC channels. J Membr Biol 1997 June 01;157(3):271-279.

(7) Bayrhuber M, Meins T, Habeck M, Becker S, Giller K, Villinger S, et al. Structure of the human voltage-dependent anion channel. Proc Natl Acad Sci U S A 2008 October 07;105(40):15370-15375.

658 (8) Hiller S, Garces RG, Malia TJ, Orekhov VY, Colombini M, Wagner G. Solution structure
659 of the integral human membrane protein VDAC-1 in detergent micelles. Science 2008 August
660 29;321(5893):1206-1210.
661 (9) Ujwal R, Cascio D, Colletier JP, Faham S, Zhang J, Toro L, et al. The crystal structure of
662 mouse VDAC1 at 2.3 A resolution reveals mechanistic insights into metabolite gating. Proc
663 Natl Acad Sci U S A 2008 November 18;105(46):17742-17747.
664 (10) Schneider R, Etzkorn M, Giller K, Daebel V, Eisfeld J, Zweckstetter M, et al. The native
665 conformation of the human VDAC1 N terminus. Angew Chem Int Ed Engl 2010 March
666 01;49(10):1882-1885.
667 (11) Zachariae U, Schneider R, Briones R, Gattin Z, Demers JP, Giller K, et al. beta-Barrel
668 mobility underlies closure of the voltage-dependent anion channel. Structure 2012 September
669 05;20(9):1540-1549.
670 (12) Geula S, Naveed H, Liang J, Shoshan-Barmatz V. Structure-based analysis of VDAC1
671 protein: defining oligomer contact sites. J Biol Chem 2012 January 13;287(3):2179-2190.
672 (13) Mertins B, Psakis G, Grosse W, Back KC, Salisowski A, Reiss P, et al. Flexibility of the
673 N-terminal mVDAC1 segment controls the channel's gating behavior. PLoS One
674 2012;7(10):e47938.
675 (14) Teijido O, Ujwal R, Hillerdal CO, Kullman L, Rostovtseva TK, Abramson J. Affixing N-
676 terminal alpha-helix to the wall of the voltage-dependent anion channel does not prevent its
677 voltage gating. J Biol Chem 2012 March 30;287(14):11437-11445.
678 (15) De Pinto V, Tomasello F, Messina A, Guarino F, Benz R, La Mendola D, et al.
679 Determination of the conformation of the human VDAC1 N-terminal peptide, a protein moiety
680 essential for the functional properties of the pore. Chembiochem 2007 May 07;8(7):744-756.
681 (16) Guardiani C, Scorciapino MA, Amodeo GF, Grdadolnik J, Pappalardo G, De Pinto V, et
682 al. The N-Terminal Peptides of the Three Human Isoforms of the Mitochondrial Voltage-

683 Dependent Anion Channel Have Different Helical Propensities. Biochemistry 2015 September
684 15;54(36):5646-5656.
685 (17) Maier JA, Martinez C, Kasavajhala K, Wickstrom L, Hauser KE, Simmerling C. ff14SB:
686 Improving the Accuracy of Protein Side Chain and Backbone Parameters from ff99SB. J Chem
687 Theory Comput 2015 August 11;11(8):3696-3713.
688 (18) Song D, Luo R, Chen H. The IDP-Specific Force Field ff14IDPSFF Improves the
689 Conformer Sampling of Intrinsically Disordered Proteins. Journal of Chemical Information and
690 Modeling 2017.
691 (19) Preto J, Clementi C. Fast recovery of free energy landscapes via diffusion-map-directed
692 molecular dynamics. Phys Chem Chem Phys 2014 Sep 28;16(36):19181-19191.
693 (20) Shen Y, Bax A. SPARTA+: a modest improvement in empirical NMR chemical shift
694 prediction by means of an artificial neural network. J Biomol NMR 2010 September
695 01;48(1):13-22.
696 (21) Hamelberg D, Mongan J, McCammon JA. Accelerated molecular dynamics: a promising
697 and efficient simulation method for biomolecules. J Chem Phys 2004 June 22;120(24):11919-
698 11929.
699 (22) Pierce LC, Salomon-Ferrer R, Augusto F. de Oliveira, Cesar, McCammon JA, Walker
700 RC. Routine access to millisecond time scale events with accelerated molecular dynamics.
701 Journal of chemical theory and computation 2012;8(9):2997-3002.
702 (23) Tian C, Kasavajhala K, Belfon KAA, Raguette L, Huang H, Migues AN, et al. ff19SB:
703 Amino-Acid-Specific Protein Backbone Parameters Trained against Quantum Mechanics
704 Energy Surfaces in Solution. J Chem Theory Comput 2020 January 14;16(1):528-552.
705 (24) Villinger S, Briones R, Giller K, Zachariae U, Lange A, de Groot BL, et al. Functional
706 dynamics in the voltage-dependent anion channel. Proc Natl Acad Sci U S A 2010 December
707 28;107(52):22546-22551.

708 (25) Rostovtseva TK, Bezrukov SM. VDAC inhibition by tubulin and its physiological
709 implications. Biochim Biophys Acta 2012 June 01;1818(6):1526-1535.
710 (26) Noskov SY, Rostovtseva TK, Chamberlin AC, Teijido O, Jiang W, Bezrukov SM. Current
711 state of theoretical and experimental studies of the voltage-dependent anion channel (VDAC).
712 Biochim Biophys Acta 2016 July 01;1858(7 Pt B):1778-1790.
713 (27) Im W, Seefeld S, Roux B. A Grand Canonical Monte Carlo-Brownian dynamics algorithm
714 for simulating ion channels. Biophys J 2000 August 01;79(2):788-801.
715 (28) Im W, Roux B. Ion permeation and selectivity of OmpF porin: a theoretical study based
716 on molecular dynamics, Brownian dynamics, and continuum electrodiffusion theory. J Mol
717 Biol 2002 September 27;322(4):851-869.
718 (29) Rui H, Lee KI, Pastor RW, Im W. Molecular dynamics studies of ion permeation in
719 VDAC. Biophys J 2011 February 02;100(3):602-610.
720 (30) Romero P, Obradovic Z, Li X, Garner EC, Brown CJ, Dunker AK. Sequence complexity
721 of disordered protein. Proteins 2001 January 01;42(1):38-48.
722 (31) Walsh I, Martin AJ, Di Domenico T, Tosatto SC. ESpritz: accurate and fast prediction of
723 protein disorder. Bioinformatics 2012 February 15;28(4):503-509.
724 (32) Wright PE, Dyson HJ. Linking folding and binding. Curr Opin Struct Biol 2009;19(1):31-
725 38.
726 (33) Meszaros B, Tompa P, Simon I, Dosztanyi Z. Molecular principles of the interactions of
727 disordered proteins. J Mol Biol 2007 September 14;372(2):549-561.
728 (34) Wang W, Ye W, Jiang C, Luo R, Chen H. New Force Field on Modeling Intrinsically
729 Disordered Proteins. Chemical Biology & Drug Design 2014;84(3):253-269.
730 (35) Robustelli P, Piana S, Shaw DE. Developing a molecular dynamics force field for both
731 folded and disordered protein states. Proc Natl Acad Sci U S A 2018 May 22;115(21):E4758-
732 E4766.

733 (36) Best RB, Zheng W, Mittal J. Correction to Balanced Protein–Water Interactions Improve
734 Properties of Disordered Proteins and Non-Specific Protein Association. Journal of Chemical
735 Theory and Computation 2015;11(4):1978.
736 (37) Bohm R, Amodeo GF, Murlidaran S, Chavali S, Wagner G, Winterhalter M, et al. The
737 Structural Basis for Low Conductance in the Membrane Protein VDAC upon beta-NADH
738 Binding and Voltage Gating. Structure 2020 February 04;28(2):206-214.e4.
739 (38) Choudhary OP, Paz A, Adelman JL, Colletier JP, Abramson J, Grabe M. Structure-guided
740 simulations illuminate the mechanism of ATP transport through VDAC1. Nat Struct Mol Biol
741 2014 July 01;21(7):626-632.
742 (39) Briones R, Weichbrodt C, Paltrinieri L, Mey I, Villinger S, Giller K, et al. Voltage
743 Dependence of Conformational Dynamics and Subconducting States of VDAC-1. Biophys J
744 2016 September 20;111(6):1223-1234.
745 (40) Blachly-Dyson E, Peng S, Colombini M, Forte M. Selectivity changes in site-directed
746 mutants of the VDAC ion channel: structural implications. Science 1990 March
747 09;247(4947):1233-1236.
748 (41) Pearlman DA, Case DA, Caldwell JW, Ross WS, Cheatham TE, DeBolt S, et al. AMBER,
749 a package of computer programs for applying molecular mechanics, normal mode analysis,
750 molecular dynamics and free energy calculations to simulate the structural and energetic
751 properties of molecules. Comput Phys Commun 1995;91(1-3):1-41.
752 (42) *Molecular Operating Environment (MOE)*, 2019.01; Chemical Computing Group ULC,
753 1010 Sherbooke St. West, Suite #910, Montreal, QC, Canada, H3A 2R7, 2020.
754 (43) Karplus M, McCammon JA. Molecular dynamics simulations of biomolecules. Nat Struct
755 Biol 2002 Sep;9(9):646-652.

(44) Wang Y, Markwick PR, de Oliveira CA, McCammon JA. Enhanced Lipid Diffusion and Mixing in Accelerated Molecular Dynamics. J Chem Theory Comput 2011 October 11;7(10):3199-3207.

(45) Miao Y, Sinko W, Pierce L, Bucher D, Walker RC, McCammon JA. Improved Reweighting of Accelerated Molecular Dynamics Simulations for Free Energy Calculation. J Chem Theory Comput 2014 July 08;10(7):2677-2689.

(46) Lomize MA, Pogozheva ID, Joo H, Mosberg HI, Lomize AL. OPM database and PPM web server: resources for positioning of proteins in membranes. Nucleic Acids Res 2012 January 01;40(Database issue):370.

(47) Jo S, Kim T, Im W. Automated builder and database of protein/membrane complexes for molecular dynamics simulations. PLoS One 2007 September 12;2(9):e880.

(48) Horvath SE, Daum G. Lipids of mitochondria. Prog Lipid Res 2013 October 01;52(4):590-614.

(49) Im W, Roux B. Ion permeation and selectivity of OmpF porin: a theoretical study based on molecular dynamics, Brownian dynamics, and continuum electrodiffusion theory. J Mol Biol 2002 September 27;322(4):851-869.

(50) Lee KI, Jo S, Rui H, Egwolf B, Roux B, Pastor RW, et al. Web interface for Brownian dynamics simulation of ion transport and its applications to beta-barrel pores. J Comput Chem 2012 January 30;33(3):331-339.